Supplementary Information for:

Elasto-Plastic Effects on Shape-Shifting Electron-Beam-Patterned Gel-Based Micro-Helices

Xinpei Wu,[1] Feiyue Teng,[1,2] Emre Firlar,[3,4] Teng Zhang,[5] and Matthew Libera[1*]

[1] Dept. of Chemical Engineering & Materials Science,
Stevens Institute of Technology, Hoboken, NJ USA

[2] presently with the Center for Functional Nanomaterials,
Brookhaven National Laboratory, Upton, NY

[3] Rutgers CryoEM & Nanoimaging Facility and Institute for Quantitative Biomedicine,
Rutgers University, Piscataway, NJ

[4] presently with Bristol Myers Squibb, Molecular Structure and Design, Princeton, NJ

[5] Dept. of Mechanical and Aerospace Engineering
Syracuse University, Syracuse, NY USA

[*] corresponding author: mlibera@stevens.edu

1. Materials and methods

Materials: Poly(acrylic acid) [PAA; average M_w = 450,000 Da; Sigma Aldrich], Phosphate Buffered Saline [PBS; Sigma Aldrich], Hydrochloric acid [ACS reagent, ⩾37.0%; HCl; Sigma Aldrich], Sodium chloride [ACS reagent, ⩾99.0%; NaCl; Sigma Aldrich], 3-(Trihydroxysilyl)-1-propanesulfonic acid (30-35% in water; Sulfonic acid-silane; Gelest], 1-ethyl-3-(3-dimethylaminopropyl)carbodiimide hydrochloride [EDC; Thermo Scientific], N-hydroxysulfosuccinimide [Sulfo-NHS; Thermo Scientific] and Cyanine3 amine [Amine-Cy3; Lumiprobe] were used as received. Type I deionized (DI) water was provided by a Millipore Direct Q system. Phosphate buffer with pH = 7.4 was prepared by diluting PBS 10 times (0.1X PBS), and phosphate buffer at pH 3.0 was prepared by adding hydrochloric acid to 0.1X PBS to adjust pH to 3.0. In both cases, the ionic strength was $[Na^+]$ = 0.0148 M.

Silane surface treatment: Silicon wafers (5 mm × 5 mm, Ted Pella) were immersed for 12 h in piranha solution (3:1 H_2SO_4/H_2O_2, use with caution), then rinsed multiple times with DI water and dried with gently flowing nitrogen gas. These wafers were then immediately exposed to an oxygen plasma for 10 min. The wafers were next immersed in 2 % (v/v) sulfonic acid-silane in ethanol for 10 min. After rinsing, the silane-treated wafers were baked in the furnace for 2 hr at 120 °C. This silanization treatment was used to impart a negative charge to the substrate surface and minimize adsorption of the shape-shifted structures. In the absence of such silanization, adsorption was frequent and would cause irrecoverable changes to the helices.

Fabrication of fluorescently labelled PAA films: Carbodiimide chemistry was used to prepare fluorescently labelled PAA. Following the manufacturer's protocol, 1 mg EDC and 1.7 mg Sulfo-NHS were added to 2 ml of PAA solution (4 wt % in methanol) to activate the carboxylic acids. The resultant mixture was sonicated for 15 min at room temperature. Then, 50 µL of amine-Cy3 solution (1 mg/ml in MES buffer) was mixed with 2 mL of activated PAA solution by vortexing. The ratio of amine-Cy3 to PAA was chosen with the target of labeling 0.005% of the PAA carboxyl groups. After 1 hr of reaction time, polymer films with a thickness of $\geq 500\ nm$ were prepared by dropping 50 µL of this labelled PAA solution onto silane-treated silicon substrates spinning at 5000 rpm for 20 s. This rotation speed is high enough to create a uniform film for high M_w PAA.

E-beam patterning: E-beam lithography was carried out using either a Zeiss Auriga or a Thermo Fisher Scientific Apreo 2S field-emission gun scanning electron microscope (FE-SEM). Both SEMs were equipped with a high-speed electron beam-blanking systems and a Nanometer Pattern Generation Systems (NPGS, JC Nabity Lithography Systems). Shape-shifting patterns were created using focused electron beams with E_o = 2 keV and a beam current of ~240 pA. The interpixel spacing along the $\hat{x}$ direction (see Fig. 2) was held constant at 2 nm. Rectangular tethering pads (20 µm x 1 µm) were then patterned using 10 keV electrons with a beam current of ~340 pA. The interpixel spacings in both $\hat{x}$ and $\hat{y}$ for

patterning the tethering pads was 200 nm. Point doses, D_p, (the total number of electrons per pixel), for patterning the shape-shifting structures ranged from 2-100 fC. Patterning a straight line with a length of 100 μm required a total exposure time on the order of 100 ms, depending on the point dose. Many such patterns of similar or greater complexity could be quickly scribed onto one sample of PAA-coated silicon. The slowest step in the processing corresponded to the electron microscope realignment required when changing the accelerating voltage from 2 keV to 10 keV. After exposure, insufficiently cross-linked polymer was removed by immersing the substrates in 2−3 mL of phosphate buffer (pH 7.4; $[Na^+]$ = 0.0148 M)) for 10 min with gentle rotary shaking (30 rpm). After rinsing twice, the patterned wafers were immersed in pH 3 or pH 7.4 phosphate buffer ($[Na^+]$ = 0.0148 M) for the subsequent imaging. The specimens were not allowed to dry. We note that patterning of dry samples demonstrated the high spatial resolution typically ascribed to e-beam lithography, mitigated by the fact that we used low accelerating voltages where beam broadening effects are more pronounced than at high (e.g. 30 kV or 100 kV) voltages often used for e-beam lithography. Since, however, our patterned dimensions changed once the samples were hydrated and the magnitude of those changes depends on factors unrelated to the patterning conditions such as pH, we did not explore what might be the smallest feature size we could produce via this approach.

Characterization: Confocal images were collected using either a Nikon Ni-E upright microscope equipped with an AxR confocal system or a Nikon E-1000 upright microscope equipped with a Nikon C1 confocal system using a Nikon Water Dipping 60X objective lens (CFI Fluor 60X W, NA 1.0 and W.D. 2.0 mm). 3D-stacked images were collected with a typical Δz step of 0.3 μm. Confocal images were extracted using the Fiji[1] image-processing software. 3D visualization and image quantification were implemented using the 3D Viewer plugin for Fiji and NIS-Elements C software. Images were collected in phosphate buffer with pH values of either 3.0 or 7.4 at a fixed ionic strength ($[Na^+]$ = 0.0148 M).

AFM images and thickness data from dry and hydrated samples were collected using a Bruker Bioscope Resolve microscope in PeakForce QNM® (quantitative nanoscale characterization) modes in air or in phosphate buffer (pH 3 or 7.4). The probes used were: (1) SCANASYST-AIR for dry samples (Silicon nitride cantilever, spring constant ≈ 0.4 N/m, tip radius ≈ 2 nm); and (2) SCANASYST-FLUID for wet samples (silicon nitride cantilever, spring constant ≈ 0.7 N/m, tip radius ≈ 20 nm). The height and modulus data were analyzed using NanoScope Analysis V1.90 software.

Finite element simulation: We performed all simulations with the ABAQUS/explicit solver. The core and corona were modeled using the anisotropic and isotropic elastic material model in ABAQUS under geometric nonlinear deformation. We assumed that the Young's moduli of the corona and core were 1 MPa and 100 MPa, respectively. The modulus of the core was then used as a tuning parameter to test the effect of mechanical anisotropic properties on the helix formation. The Poisson ratios of the core and corona

were assumed to be 0.3 and 0.4, respectively. The swelling behaver of the corona was modeled as a volumetric expansion and implemented through the thermal expansion function in ABAQUS. The composite rods were discretized using 8-node linear brick elements (C3D8R). The mesh size was close to 40 nm. The total simulation time was 5 ms, during which the volumetric swelling ratio of the corona linearly increased from 0 to 3.375. A mass scaling technique was adopted to accelerate the simulation speed. During the simulation, the left end of the of the rod was fixed, and the rest of the rod was free to move. A general contact interaction in Abacus was used to prevent material penetration.

2. Monte Carlo Simulation

The interaction of energetic electrons with PAA films was modelled using a Monte Carlo simulation.[2, 3] Single-electron trajectories were followed, and various decisions along these trajectories about the scattering type (elastic or inelastic), scattering angle, and energy change due to electron-nuclei interactions were made using a random-number generator weighted by a screened Rutherford elastic cross section. This approach followed well-established methods described by David Joy with the algorithms coded using MATLAB [(2020) version 9.8.0 *(R2020a)*. Natick, Massachusetts: The MathWorks Inc.].

Energy deposition into the PAA was accounted for via the modified Bethe model for the stopping power, S (eV/Å):[2, 4]

$$S = -\frac{dE}{ds} = 785\frac{\rho Z}{AE} ln\left[\frac{1.166(E+kJ)}{J}\right] \quad ...[S1]$$

where E is the instantaneous electron energy (eV) and s represents a distance along the trajectory of the electron. ρ, Z, A, and J are the density (g/cm^3), atomic number, atomic weight (g/mole), and mean ionization potential (eV), respectively. The values used for these latter parameters are given in Table S1. Z and A were determined based on a weighted average of the atoms present [5] for the PAA monomer stoichiometry of $C_3H_4O_2$. The mean ionization potential was estimated using the relation J=11.5Z.[4] The parameter k was assumed to be 0.85.[2] Figure S1 describes the stopping power of PAA as a function of electron energy using eq. [S1] and the parameters in Table S1. This model agrees reasonably well with data in the literature at higher energies (above ~500 eV). However, it likely overestimates the stopping power at low energies (~5-50 eV) where there is relatively little experimental data to guide the model and its parameters.

Table S1 - Parameters used in Monte Carlo simulation

ρ	1.21	g/cm^3
Z	6.56	
A	14.15	g/mole
J	75.44	eV

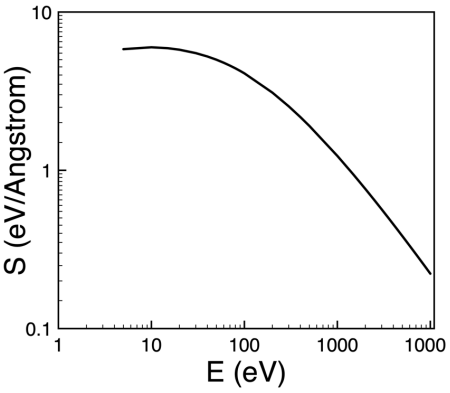

Fig. S1: The electron stopping power for PAA calculated using the modified Bethe model (eq. [S1]).

Individual electron trajectories were followed until the energy of the electron fell below 5 eV or until an electron reached the top surface of the specimen, (x, y, z = 0), where it escaped into the surrounding vacuum. In the former case, the remaining 5 eV of energy was

ignored. Prior to this end point, the electron energy loss between scattering events due to the continuous slowing down of the electron in the specimen - given by the product of the instantaneous stopping power and the distance between successive scattering events – was accumulated in an 8 nm^3 voxel at the end of the corresponding linear segment of the electron trajectory. These simulations were carried out for incident electron energies of 2 keV (shape-shifting structure) and 10 keV (tethering pad) and for various incident electron point doses ranging from 1 fC to 100 fC. All incident electrons were assumed to initially travel in the z direction and to impinge on the specimen at the point (0, 0, 0).

3. Modeling the swelling of E-beam patterned

We combined the results of Monte Carlo simulations of energy deposition with a gel-swelling model to estimate both the nature of the asymmetric swelling within irradiated PAA and the effect of pH on that swelling.

The MC simulations generated 3-dimensional arrays representing the magnitude of energy deposited (eV) within a voxel of size 2 nm x 2 nm x 2 nm. We then converted that energy deposition into an indicator of the resulting radiation chemistry. Notably, Winzor et al. have studied the radiation chemistry for γ-irradiated PAA.[6, 7] They report a G_x value - the number of crosslinking events per 100 eV of deposited energy - of 0.44 while that for chain scission, G_s, is close to zero. Thus, a radiation-driven increase in molecular weight (cross linking) is far more likely than a decrease (chain scission). Crosslinking in PAA is believed to occur by a free-radical mechanism caused either by direct knock-on or hydroxyl-driven removal of hydrogen from a main-chain carbon atom.[7-9] Winzor et al. furthermore show that the G_{COOH} value for damaging the PAA carboxyl group is approximately 27 times higher than G_x: $G_{COOH} = G_{CO2} + G_{CO} = 12$. Radiation-induced CO/CO_2 release effectively converts acid-like monomers into ethylene-like monomers and is manifested as mass loss from the precursor film. Using G_x=0.44, a characteristic ratio of 6.7 [10] and assuming Gaussian conformations in the solid PAA film, the average energy density to create a crosslink in solid 450 kDa PAA is 0.33 eV/nm^3. The energy deposited per voxel could then be converted into a measure of the number of crosslinks per voxel.

The volumetric swelling ratio (Q) was calculated by using an expression developed by Jia and Muthukumar[11] for polyelectrolyte gels with low concentrations of excess salt:

$$-ln(1-\varphi) - \varphi - \chi\varphi^2 + \alpha z_p \varphi = \frac{1}{N}\left(\varphi_o^{2/3}\varphi^{1/3} - \frac{\varphi}{2}\right) \quad \text{...[S2]}$$

where:

$\varphi = the\ volume\ fraction\ of\ polymer$

$\varphi_o = the\ volume\ fraction\ of\ polymer\ in\ a\ reference\ state$

$\chi = the\ Flory - Huggins\ interaction\ parameter$

$N = the\ number\ of\ Kuhn\ monomers\ between\ crosslinks$

$\alpha = the\ fraction\ of\ ionized\ groups\ per\ Kuhn\ monomer$

$z_p = the\ electrostatic\ charge\ per\ Kuhn\ monomer$

At equilibrium: $Q = \frac{1}{\varphi}$.

Since our focus was to illustrate the effect of pH on the relative swelling, we made a number of assumptions. We assumed that $\varphi_o = 1$, and we modeled the chain using the chemical monomer rather than the Kuhn monomer. With pK_a=4.5 for PAA[12], we assumed the PAA acid groups to be fully protonated at pH 3 ($\alpha = 0$). In this case, the Jia-Muthukumar formulation recovers the classical Flory-Rehner model.[13] We assumed that the acid groups are fully deprotonated at pH 7.4 whereupon $\alpha = 0.32$ and $z_p = 1$.[14] We used a value of $\chi = 0.41$ [15].

In addition to crosslinking, Winzor et al[7] have shown that exposure to radiation not only causes crosslinking but also damages the acid groups within PAA. They report a G value for this damage as: $G_{COOH} = G_{CO2} + G_{CO} = 12$. $G_{COOH}/G_x = 12/0.44 = 27.3$, which indicates that, on average, 27 monomer units are damaged for each monomer unit that undergoes crosslinking. Since the G value for chain scission in PAA is very small,[13, 16], we assume that this damage essentially converts an acrylic acid monomer into a hydrophobic moiety resembling something like a polyethylene monomer. Hence, we calculated an effective number of swellable monomers between crosslinks via the expression:

$$N = (N_{max} - 27n)/n \qquad \text{...[S3]}$$

where n is the number of crosslinks per molecule and N_{max} = the total number of monomers in a given molecule. For PAA with M_w = 450 kDa, N_{max} = 6250. $N_{max}/27 = 231$ is thus the maximum number of crosslinking events that can occur in a given molecule before this simple model predicts that all PAA monomers have been converted to something that no longer resembles acrylic acid.

Given an amount of energy deposited in a particular voxel, we calculated the number of crosslinking events per molecule within that voxel. We corrected for the damage using eq. [S3] and then used eq. [S2] to calculate $Q=1/\phi$ for that voxel at pH 3 and pH 7.4. We note that this approach evaluates the swelling of each voxel independent of the voxels surrounding it. An even more accurate model would further correct for the additional mechanical constraints of the local environment.

4. Symmetric double line experiments for D_p = 10 fC and D_p = 40 fC.

D_p = 10 fC

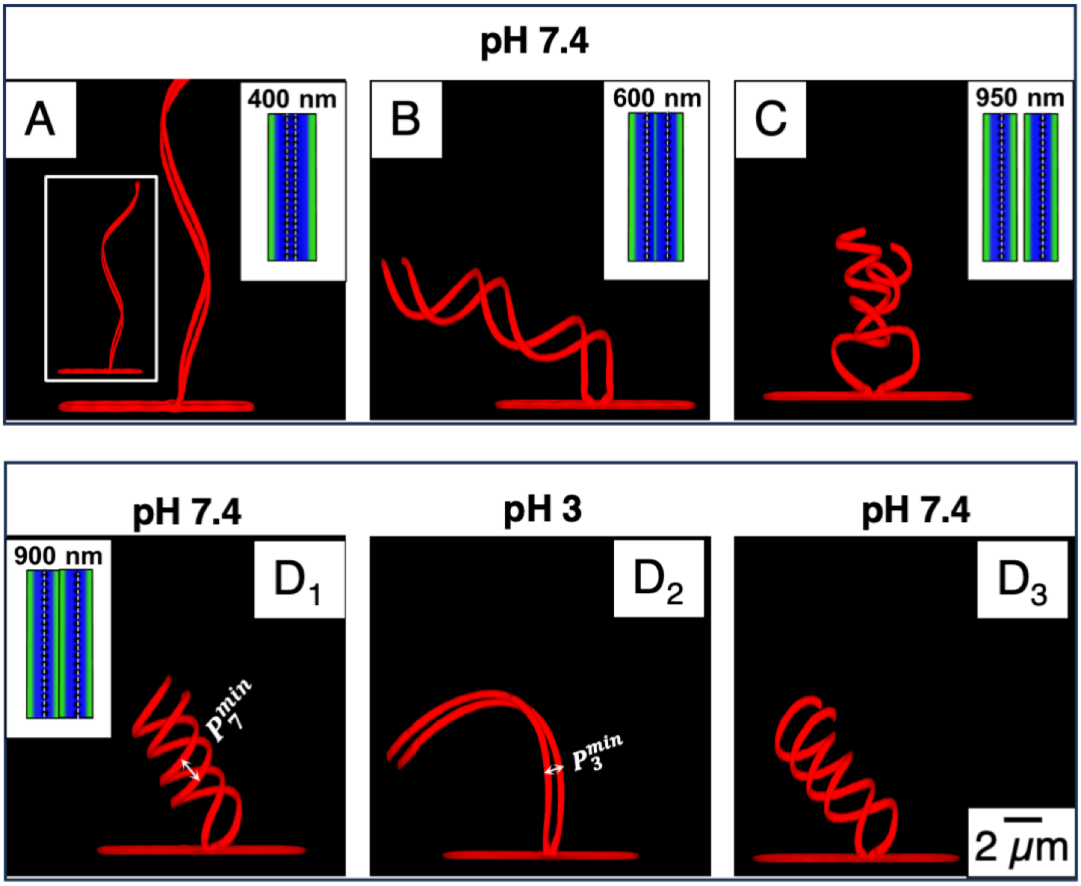

Fig. S2: Parallel lines separated by a distance Δy shape shift into single helices (A: Δy = 400 nm), double helices (B: Δy = 600 nm & D: Δy = 900 nm), and two independent helices (C: Δy = 950 nm) depending on the magnitude of Δy. All lines were patterned using D_p = 10 fC, δ_x = 2 nm, and L_o = 50 μm. The pH of the imaging buffer is indicated.

D_p = 40 fC

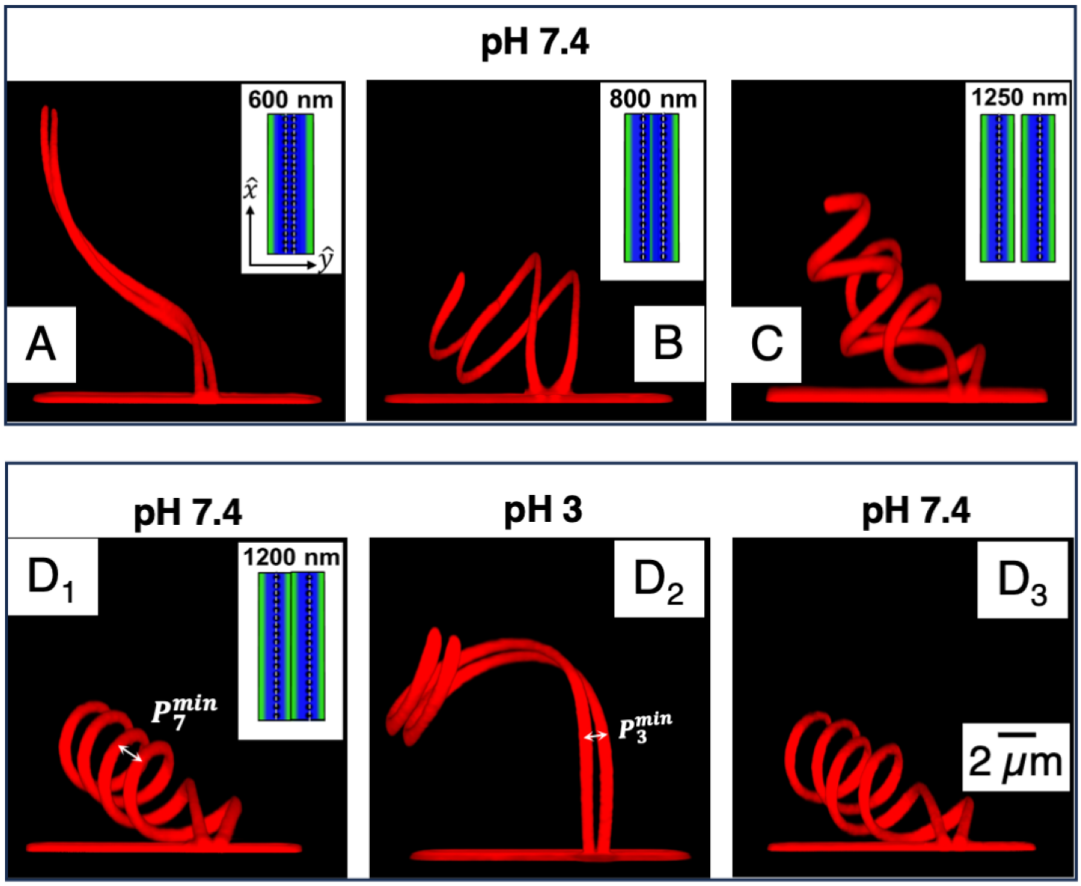

Fig. S3: Parallel lines separated by a distance Δy shape shift into single helices (A: Δy = 600 nm), double helices (B: Δy = 800 nm & D: Δy = 1200 nm), and two independent helices (C: Δy = 1250 nm) depending on the magnitude of Δy. All lines were patterned using D_p = 40 fC, d_x = 2 nm, and L_o = 50 μm. The pH of the imaging buffer is indicated.

5. *In situ* wide-field fluorescence imaging of the pH-induced shape change.

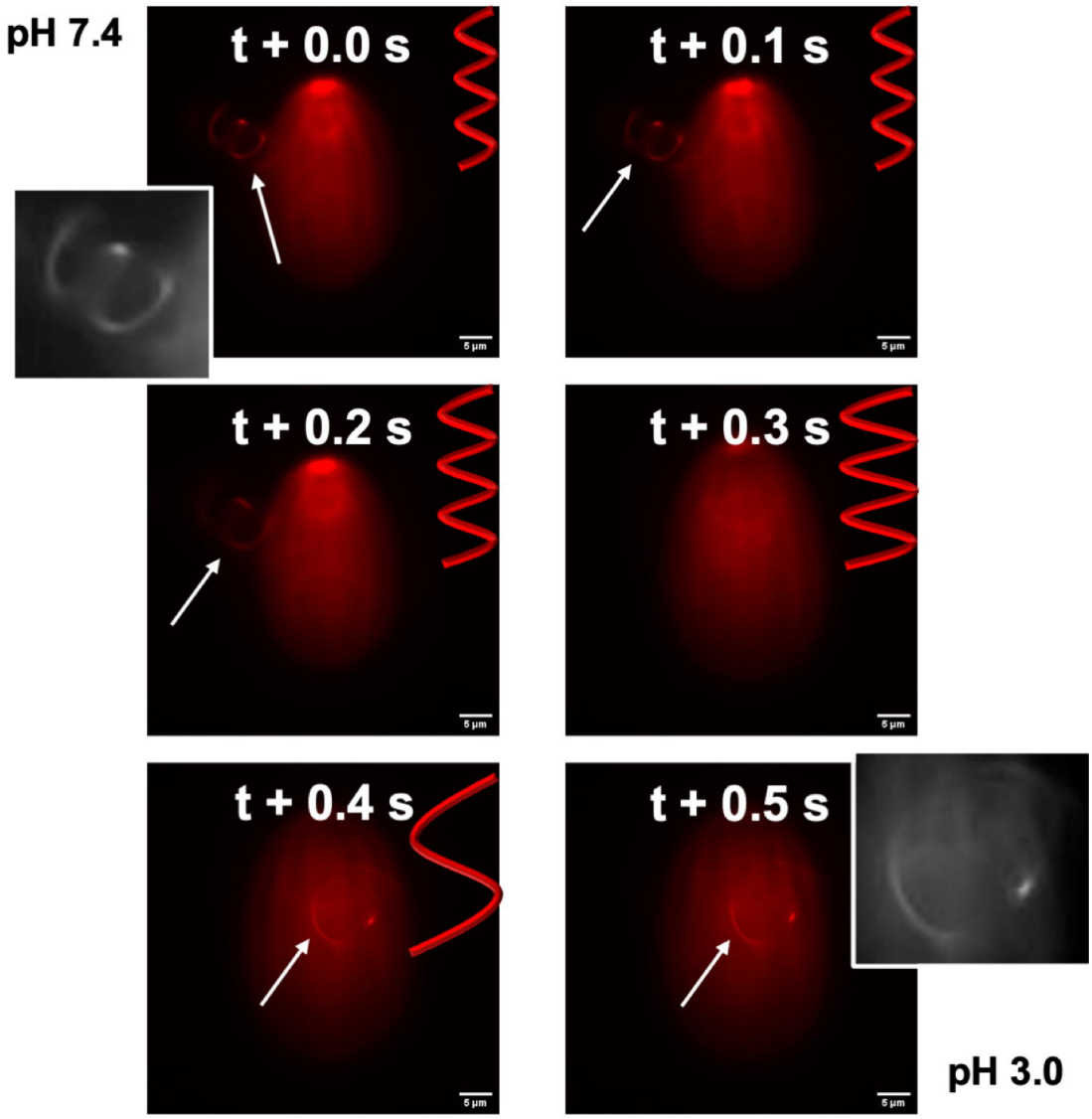

Figure S4: A time-resolved sequence of images showing the transformation of a PAA helix when the pH is changed from 7.4 to 3.

These are wide-field fluorescence images, not confocal, and only one plane within the 3D volume of the helix is in focus. In each image, the white arrow indicates a portion of the helix that is in focus. The sequence shows that the helical radius increases from smaller to larger over the image series. The black and white insets indicate the before/after curvature.

The images were collected at 100 ms time intervals. The transformation begins between 0.1/0.2 s and ends between 0/3/0.4 s. The helix moves both because of intrinsic forces due to the transformation and because of fluid flow during the buffer exchange.

The inset schematic diagrams in the upper right corner of each image illustrate shape change qualitatively.

6. pH-cycling data

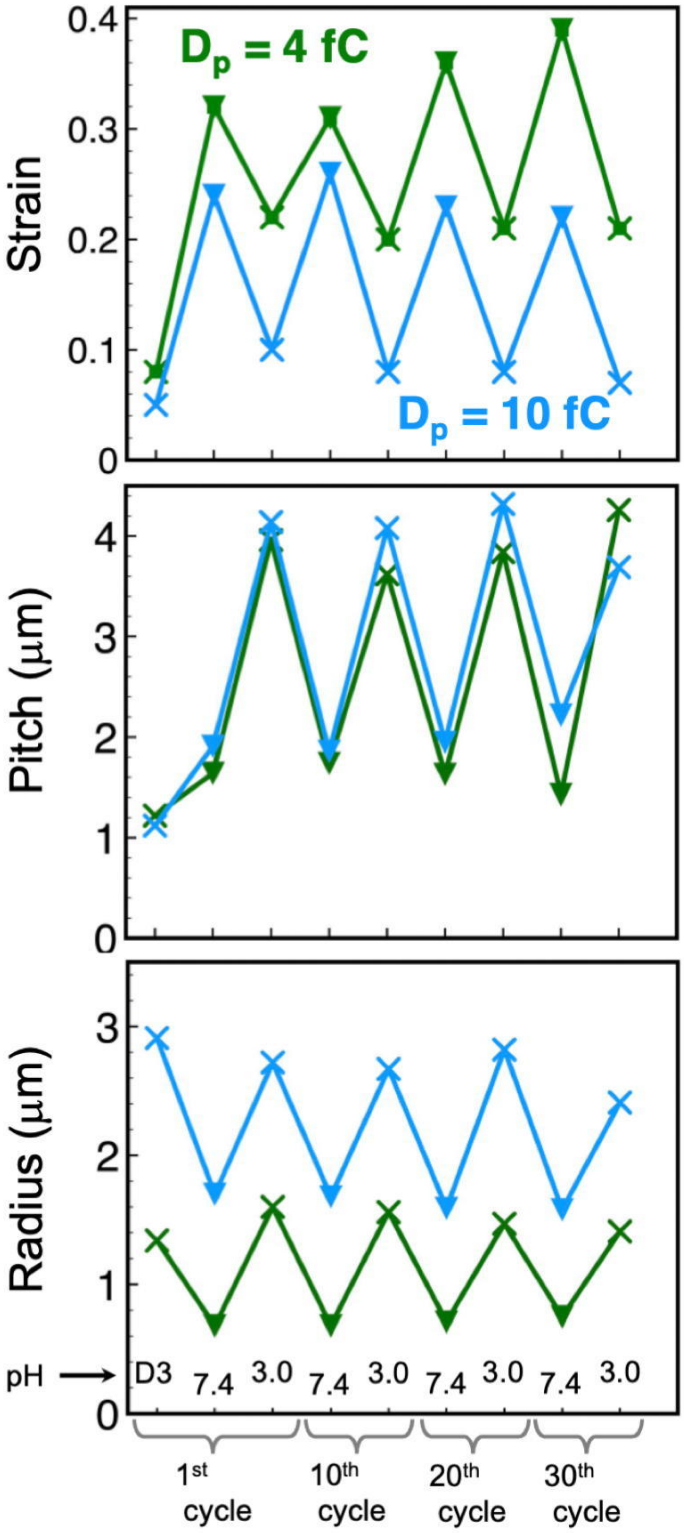

Fig. S5: Helices patterned using point doses of 4 fC (green) and 10 fC (blue) were cycled between phosphate buffers at pH 3.0 (X) and pH 7.4 (▼) 30 times.

7. Aging at pH 7.4

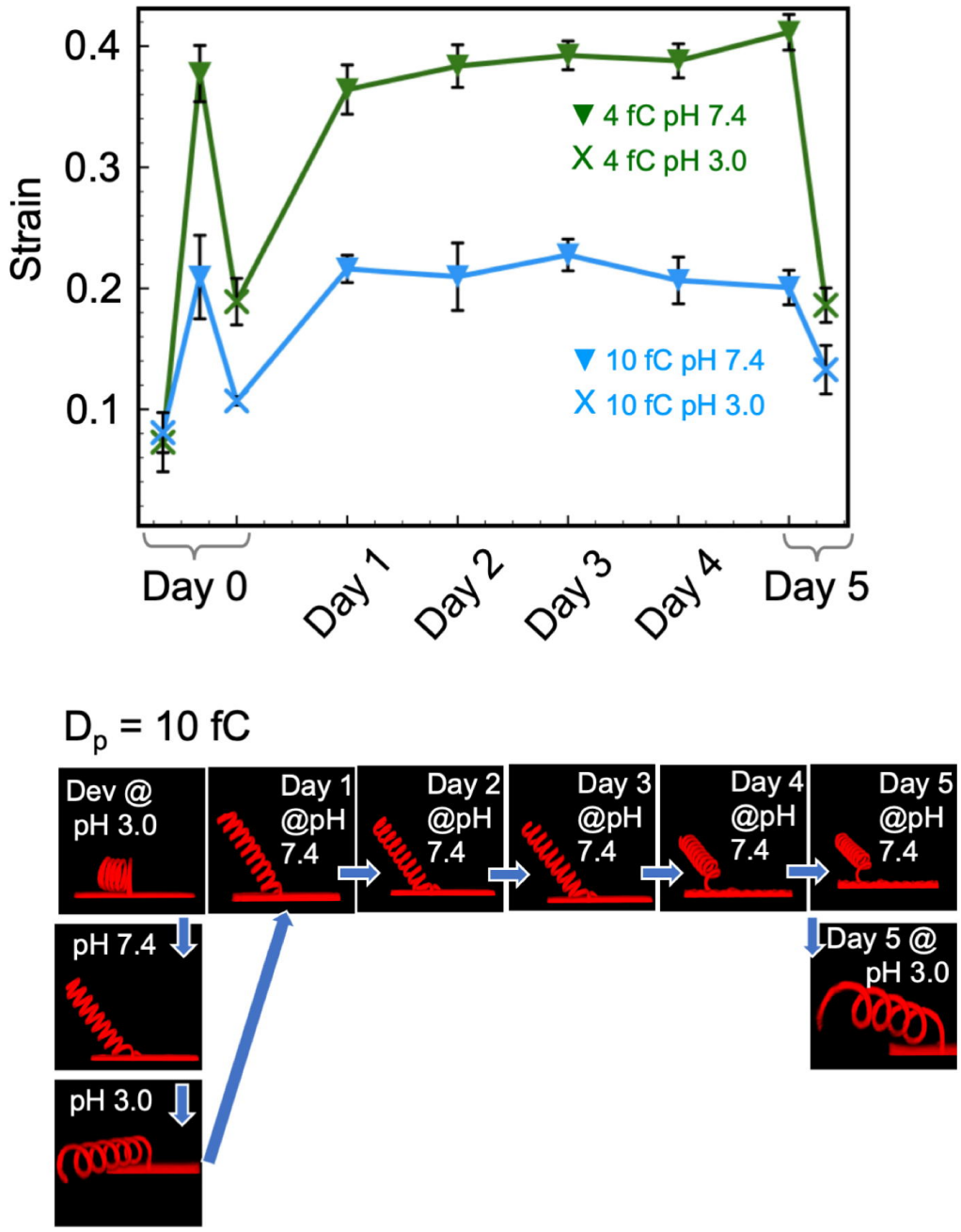

Fig. S6: Aging in pH 7.4 buffer for five days does not recover the initial plastic deformation induced by the initial excursion in pH from 3.0 to 7.4 on Day 0.

8. Effect of 45º line orientation on chirality

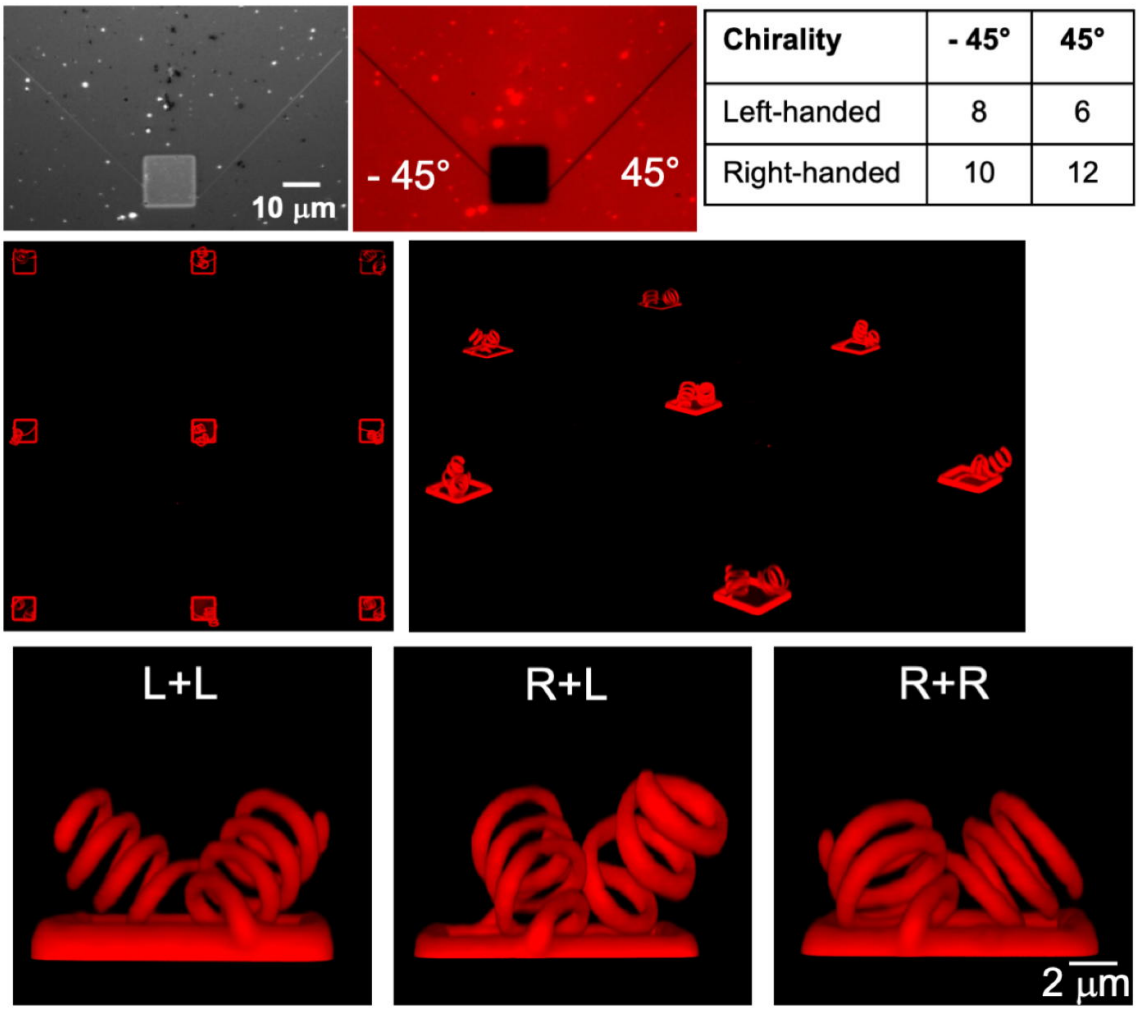

Chirality	- 45°	45°
Left-handed	8	6
Right-handed	10	12

Fig. S7: Patterning a line at a 45° angle relative to a square tethering pad generates random chirality. (Top) Wide-angle bright-field (top left) and fluorescence (top right) images of as-patterned lines (D_p = 10 fC) oriented 45° to the edges of a square tethering pad. (Middle) Low-magnification confocal fluorescence images of an array such patterns developed and imaged in pH 3.0 buffer. (Bottom) Higher-magnification images of structures illustrating different chirality combinations for identically patterned structures.

The table at the top right summarizes the occurrence of different chiralities for the two different line orientations and indicates no preferred orientation-based chirality (n=18).

References for Supplementary information

(1) Schindelin, J.; Arganda-Carreras, I.; Frise, E.; Kaynig, V.; Longair, M.; Pietzsch, T.; Preibisch, S.; Rueden, C.; Saalfeld, S.; Schmid, B.; et al. Fiji: an open-source platform for biological-image analysis. *Nature Methods* **2012**, *9* (7), 676-682. DOI: 10.1038/nmeth.2019

(2) Joy, D. C. *Monte Carlo Modeling for Electron Microscopy and Microanalysis*; Oxford University Press, 1995.

(3) Shimizu, R.; Ze-Jun, D. Monte Carlo modelling of electron-solid interactions. *Reports on the Progress in Physics* **1992**, 487-531.

(4) Joy, D. C.; Luo, S. An empirical stopping power relationship for low-energy electrons. *Scanning* **1989**, *11* (4).

(5) Joy, D. C.; Luo, S.; Gauvin, R.; Hovington, P.; Evans, N. Experimental measurements of electron stopping power at low energies. *Scanning Microsc.* **1996**, *10* (3), 653-666, Article.

(6) Moad, C. L.; Winzor, D. J. Quantitative characterization of radiation degradation in polymers by evaluation of scission and cross-linking yields. *Progress in Polymer Science* **1998**. DOI: 10.1016/s0079-6700(97)00041-5

(7) Hill, D. J. T.; O'Donnell, J. H.; Winzor, C. L.; Winzor, D. J. Evaluation of scission and crosslinking yields in γ-irradiated poly(acrylic acid) and poly(methacrylic acid) from weight- and Z-average molecular weights determined by sedimentation equilibrium. *Polymer* **1990**, *31* (3), 538-542, Article. DOI: 10.1016/0032-3861(90)90399-J

(8) Jeong, J. O.; Park, J. S.; Kim, E. J.; Jeong, S. I.; Lee, J. Y.; Lim, Y. M. Preparation of radiation cross-linked poly(Acrylic acid) hydrogel containing metronidazole with enhanced antibacterial activity. *Int. J. Mol. Sci.* **2020**, *21* (1), Article. DOI: 10.3390/ijms21010187

(9) Sheikh, N.; Jalili, L.; Anvari, F. A study on the swelling behavior of poly(acrylic acid) hydrogels obtained by electron beam crosslinking. *Radiation Physics and Chemistry* **2010**, *79* (6), 735-739. DOI: 10.1016/j.radphyschem.2009.12.013

(10) Plavsik, M. Configurational Statistics of Poly(acrylic acid). *Croatia Chemica Acta* **1987**, *60* (1), 129-137.

(11) Jia, D.; Muthukumar, M. Theory of Charged Gels: Swelling, Elasticity, and Dynamics. *Gels* **2021**, *7* (2). DOI: 10.3390/gels7020049

(12) Xiao, X.; Ji, J.; Zhao, W.; Nangia, S.; Libera, M. Salt Destabilization of Cationic Colistin Complexation within Polyanionic Microgels. *Macromolecules* **2022**, *55* (5), 1736-1746, Article. DOI: 10.1021/acs.macromol.1c02157

(13) Flory, P. J.; Jr., J. R. Statistical Mechanics of Cross-Linked Polymer Networks II. Swelling. *The Journal of Chemical Physics* **1943**, *11* (11), 521-526. DOI: 10.1063/1.1723792

(14) Swift, T.; Swanson, L.; Geoghegan, M.; Rimmer, S. The pH-responsive behaviour of poly(acrylic acid) in aqueous solution is dependent on molar mass. *Soft Matter* **2016**, *12* (9), 2542-2549, Article. DOI: 10.1039/c5sm02693h

(15) Colby, R. H. Elastic Modulus and Equilibrium Swelling of Polyelectrolyte Gels. *Macromolecules* **1999**.

(16) Moad, C. L.; Winzor, D. J. Quantitative characterization of radiation degradation in polymers by evaluation of scission and cross-linking yields. *Progress in Polymer Science (Oxford)* **1998**, *23* (5), 759-813, Review. DOI: 10.1016/S0079-6700(97)00041-5